The Astrophysical Journal, 948:66 (14pp), 2023 May 1 https://doi.org/10.3847/1538-4357/acc028

Turbulence and Diffusive Transport of Cosmic Rays in the Very Local Interstellar Medium

V. Florinski[1], J. G. Alonso Guzman[1], J. Giacalone[2], J. A. le Roux[1], and M. Opher[3]
[1] Department of Space Science and Center for Space Plasma and Aeronomic Research, University of Alabama in Huntsville, Huntsville, AL 35899, USA; vaf0001@uah.edu
[2] Department of Planetary Sciences and Lunar and Planetary Lab, University of Arizona, Tucson, AZ 85721, USA
[3] Department of Astronomy, Boston University, Boston, MA 02215, USA
Received 2022 November 30; revised 2023 February 13; accepted 2023 February 27; published 2023 May 8

Abstract

We study the transport of fast charged particles, such as galactic cosmic rays, in the very local interstellar medium (VLISM), which is currently being explored by the two Voyager space probes. Guided by the observations of magnetic fluctuations, the paper develops a simple theoretical framework for computing scattering rates and spatial diffusion coefficients that can be used to model cosmic-ray transport in the VLISM. The local interstellar magnetic turbulence is represented as a superposition of (a) Alfvénic, (b) transverse 2D, and (c) longitudinal components obeying distinctive geometry rules in the plasma frame. The model is based on the weakly nonlinear formalism where particle trajectory's deviation from the unperturbed helix is caused primarily by guiding-center diffusion across the mean magnetic field. The transverse component plays the dominant role in perpendicular diffusion, while the longitudinal component has only a minor effect. Pitch-angle scattering is extremely weak in the VLISM, so that cosmic-ray transport can be considered essentially scatter-free on heliospheric scales. We test our theoretical model with the help of particle orbit simulations to find good agreement for perpendicular diffusion. We also find that cosmic rays disperse faster than in a conventional random walk (diffusive) process if the turbulence power spectrum contains fluctuations whose wavelength is larger than the size of the heliosphere.

Unified Astronomy Thesaurus concepts: Heliosphere (711); Galactic cosmic rays (567); Interstellar magnetic fields (845)

1. Introduction

The outer heliosheath (OHS) is the region of space between the heliopause (HP) and the bow shock or wave formed ahead of the Sun's trajectory through the local interstellar cloud (Baranov et al. 1976; Wallis & Dryer 1976). While the region itself is interstellar in origin, its properties are very different from those of the "unperturbed" local interstellar medium (LISM) environment (Redfield & Linsky 2004; Frisch 2007). The plasma flow is parted by the presence of the obstacle (the HP) while the interstellar magnetic field is said to be "draped" around the surface of the HP (Pogorelov et al. 2011; Opher & Drake 2013; Izmodenov & Alexashov 2020), and its direction is markedly different from that in the LISM. The plasma is also heated by virtue of passing through the bow wave and the subsequent compression as well as by the addition of heat from the charge exchange with energetic hydrogen atoms produced in the inner heliosheath (IHS; the region between the termination shock and the HP). The term "VLISM," or very local interstellar medium, often used in the literature to describe the perturbed LISM region, can be considered a synonym for "OHS." According to the models (e.g., Izmodenov & Alexashov 2020), the extent of this region is a few hundred astronomical unit in the upwind direction.

Both Voyager space probes are currently traveling through the VLISM, providing humanity with its first glimpse into the properties of our solar system's interstellar environment. Observations revealed that the OHS has a plasma number density of 0.04–0.12 cm^{-3} (Gurnett et al. 2013; Gurnett & Kurth 2019) and temperature in excess of 30,000 K (Richardson et al. 2019). Measured values of the magnetic field magnitude were between 4 and 6 μG, giving values of the ion plasma beta between 0.3 and 0.65 (Burlaga & Ness 2016). Given the limited spatial coverage of the Voyager observations, these parameters are not necessarily characteristic of the VLISM as a whole, but they are broadly consistent with the results of large-scale MHD models that cover the entire heliosphere. We can, however, say with a high degree of confidence that the nearby interstellar region is drastically different from the more familiar solar wind when it comes to the properties of turbulent magnetic fluctuations. While the solar-wind plasma is mostly turbulent on sub-astronomical unit scales, the VLISM has comparatively little power in magnetic fluctuations of that size (see below). This creates a vast difference in the transport patterns of energetic particles between these two space environments.

The magnetic field is by and large turbulent in the supersonic solar wind (e.g., Burlaga 1984; Goldstein et al. 1995). The region behind the termination shock is very turbulent (Burlaga & Ness 2009a), although the amplitude of the fluctuations has decreased as Voyagers penetrated deeper into the IHS. Past the HP, however, magnetic fluctuations became extremely weak. Burlaga et al. (2015) used daily averaged values of the magnetic field vector measured by Voyager 1 between 2013.36 and 2014.64 (V1 Interval 1), the period that was devoid of shocks and other disturbances, to compute the power spectral density (PSD) of magnetic fluctuations on timescales >1 day (their analysis was limited to longer intervals by the gaps in the data due to an intermittent spacecraft downlink pattern). As reported in that study, almost half of the total power $\langle \delta B^2_{\rm obs} \rangle$ was

observed to be in the compressive or longitudinal component with the variance direction parallel to the mean magnetic field vector $\boldsymbol{B}$ (here and below we will use the prefix δ for turbulent quantities, while the large-scale background fields will be prefix-free), and the power spectra in the three components could be well fit by a $-5/3$ power-law characteristic of the inertial range. The PSD was nonetheless a factor of 100 higher than the spectrum of ambient interstellar fluctuations in the measured range of wavenumbers (see Armstrong et al. 1995; Fosalba et al. 2002; Haverkorn et al. 2008). The observed fluctuations are therefore unlikely to be of interstellar origin. Zank et al. (2017) suggested that the compressive component could be fast magnetosonic waves produced from the refraction of waves incident on the HP from the heliospheric side.

Burlaga et al. (2018) examined another 468 day period of Voyager 1 data from 2015.40 to 2016.68 (V1 Interval 2). The total spectral power in that interval was about a factor of 2 higher than in Interval 1, and the fluctuations were primarily transversely polarized, as in the solar wind. Zank et al. (2019) suggested that transverse fluctuations could be produced by nonlinear interaction between compressive fluctuations and 2D structures. However, the power in the compressive component remained about the same as in the first interval, so it is not clear whether such a transfer is energetically feasible. The transverse fluctuations might also be the consequence of large-scale instabilities of the HP, as suggested by Burlaga et al. (2018). By using 48 s averaged Voyager 1 magnetic field measurements, Fraternale et al. (2019) and Fraternale & Pogorelov (2021) extended the turbulent power spectra to higher frequencies and evaluated higher-order moments and intermittencies. They found that the spectra were consistent with $-5/3$ power laws except at short scales, where they observed some spectral flattening.

A third period (V1 Interval 3) between 2018.20 and 2019.49 was studied in Burlaga et al. (2020). The fluctuations were even stronger than during Interval 2 but otherwise similar to it with the dominant transverse component. The power in the longitudinal component remained about the same as in Intervals 1 and 2. The same paper reported Voyager 2 observations over the period 2018.85–2019.63 (V2 Interval 1). Three abrupt magnetic field increases occurred during that time, so the interval was not exactly quiet. Similar to Voyager 1 observations close to the HP, the fluctuations had a significant longitudinal component, and their PSD could be fitted with a $-5/3$ power law, with some exceptions. An update was published in Burlaga et al. (2022), but the available data set was insufficient to determine the radial evolution of turbulent fluctuations in the Voyager 2 direction.

Lee & Lee (2019, 2020) analyzed electron density fluctuations inferred from the frequency of the electrostatic plasma waves measured by Voyager 1's PWS instrument. Their study covered 2012–2019, which corresponds to the Voyager travel distance of some 24 au. Many of the periods analyzed could be characterized as "disturbed" because plasma waves are often associated with shocks (Gurnett et al. 2015). A comparison between the power spectra of magnetic and density fluctuations was also performed. While both featured Kolmogorov power-law slopes, the amplitude of density fluctuations was too small compared with the amplitude of longitudinal magnetic fluctuations, which contradicts their interpretation as magnetosonic waves, given the relatively small value of the plasma beta in the VLISM.

The scattering rates of cosmic rays in the VLISM are very low. This is supported by the observations that the heliospheric particles are apparently leaving the HP region very quickly as evidenced by their rapid intensity decrease following he HP crossings by both Voyagers (Florinski et al. 2013, 2015; Krimigis et al. 2013, 2019). In addition, galactic cosmic-ray (GCR) distributions were anisotropic for periods of time lasting several months to a year (Kóta & Jokipii 2017; Rankin et al. 2019, 2020), pointing to a lack of scattering on such temporal scales. Some workers use extremely large parallel mean free paths (MFPs; Zhang & Pogorelov 2020) to simulate the 90° notches in the distribution functions following the passage of a traveling shock wave. Our analysis shows that the parallel MFP in the VLISM is indeed large by heliospheric standards, and GCR transport in the OHS can be considered essentially scatter-free.

There is some evidence that diffusion across the magnetic field is very weak in the VLISM (Guo & Florinski 2014; Luo et al. 2016), which is required to reproduce the narrow step increase across the HP observed by Voyager 1 (Stone et al. 2013; Cummings et al. 2016). While this could be the case very close to the HP, we argue below that perpendicular diffusion could be relatively strong on large scales in the VLISM. In this paper we derive the perpendicular diffusion coefficient of GCRs by extending existing weakly nonlinear theories to include longitudinal magnetic fluctuations. The model we developed is constrained by the observed frequency-domain power spectra of magnetic fluctuations, from which we deduce the plasma-frame wavenumber PSDs that can be directly used in transport modeling. The model could be applied under typical conditions in the OHS, but should not be used without modification inside the HP transition layer. Theoretical predictions are tested with the help of particle orbit simulations in a fluctuating field characteristic of the VLISM conditions. While several broad inferences will be made, more advanced and precise measurements of the turbulent geometry than what is possible with Voyager instruments would be ultimately required to properly constrain the transport of cosmic rays in nearby interstellar space.

2. From Fluctuations to Scattering and Diffusion

Cosmic-ray transport may be thought of as a combination of scattering against traveling magnetic irregularities in a moving plasma background combined with stochastic drift motions across the mean magnetic field. A sufficiently general Fokker–Planck (FP) equation governing the evolution of the gyrotropic part $f(\boldsymbol{r}, p, \mu, t)$, μ being the pitch-angle cosine, of the cosmic-ray distribution function may be written in the form

$$\frac{df}{dt} = \frac{\partial}{\partial\mu}\left(D_{\mu\mu}\frac{\partial f}{\partial\mu} + D_{\mu p}\frac{\partial f}{\partial p}\right) + \nabla\cdot\left[D_{\perp}(\boldsymbol{I} - \hat{\boldsymbol{b}}\hat{\boldsymbol{b}})\cdot\nabla f\right] + \frac{1}{p^2}\frac{\partial}{\partial p}\left[p^2\left(D_{p\mu}\frac{\partial f}{\partial\mu} + D_{pp}\frac{\partial f}{\partial p}\right)\right], \quad (1)$$

where $\boldsymbol{I}$ is the unit tensor and $\hat{\boldsymbol{b}}$ is the unit vector in the direction of $\boldsymbol{B}$. The left-hand side contains the full derivative taken along the characteristics of the underlying transport model that involves gradients with respect to both spatial and momentum coordinates and in principle contains the effects of

large-scale drifts. Here we are interested in the right-hand side that describes the physics of pitch-angle scattering, perpendicular diffusion, and momentum diffusion. The various FP coefficients $D_{\mu\mu}$, $D_{\mu p}$, $D_{\perp}$, etc. describe diffusive transport in the respective directions; they are functions of momentum p and pitch angle μ. Later we will also deal with diffusion coefficients $\kappa_{\parallel}$ and $\kappa_{\perp}$ obtained from the FP coefficients by the appropriate pitch-angle averaging procedure. The form of the FP tensor used in (1) implies that the turbulence is both axisymmetric and helicity-free.

The focus of this paper is on relatively energetic particles whose speed is a significant fraction of the speed of light. The momentum change terms in Equation (1) are mainly due to the effects of the differential and/or stochastic motion of scattering centers relative to the plasma frame (Schlickeiser 1989). They are proportional to the turbulent electric field $\delta\boldsymbol{E} = -(\delta\boldsymbol{u} \times \boldsymbol{B} + \boldsymbol{V}_w \times \delta\boldsymbol{B})/c$, where $\delta\boldsymbol{u}$ is the turbulent velocity field and $\boldsymbol{V}_w$ is the background wave phase velocity field (e.g., in the directions parallel and antiparallel to the mean magnetic field for the Alfvén waves). As such, they scale with the ratio between the u or $V_w \sim V_A$ (the Alfvén speed) and the particle speed v according to

$$D_{\mu\mu} \sim 1,\ D_{\perp} \sim 1,\ D_{\mu p} = D_{p\mu} \sim \left(\frac{V_w}{v}\right),\ D_{pp} \sim \left(\frac{V_w}{v}\right)^2. \quad (2)$$

Typical values of V_w in the VLISM are 20–40 km s^{-1} so even at the low end of the GCR energy range the ratio $V_w/v \sim 10^{-3} \ll 1$. This means that when modeling GCRs, only $D_{\mu\mu}$ and $D_{\perp}$ are relevant. The retained terms depend only on the statistical properties of the turbulent magnetic field $\delta\boldsymbol{B}$ and not on $\delta\boldsymbol{u}$. The corresponding diffusion coefficients are given by

$$\kappa_{\parallel} = \frac{v^2}{8}\int_{-1}^{1} \frac{(1-\mu^2)^2}{D_{\mu\mu}} d\mu, \quad (3)$$

$$\kappa_{\perp} = \frac{1}{2}\int_{-1}^{1} D_{\perp} d\mu. \quad (4)$$

It should be noted that diffusion is only one (although common) possibility, defined in simplest terms as a random walk process, where the mean square displacement from the source increases linearly with time. More generally, the mean square displacement can be a power law in time t^{α} with an index α less than one (subdiffusion) as well as greater than one (superdiffusion). Subdiffusion could occur in systems with at least one ignorable coordinate (Jokipii et al. 1993; Jones et al. 1998). In pure slab turbulence, scattering and field-line meandering processes could combine to yield compound perpendicular diffusion with $\alpha = 1/2$ (Kóta & Jokipii 2000; Qin et al. 2002). Superdiffusive behavior with $\alpha > 1$ is expected on timescales shorter than the characteristic time for the particles to traverse the outer scale of the turbulence, i.e., before the diffusive regime could be established (Lazarian & Yan 2014). In this paper we will encounter both of these scenarios.

Returning now to ordinary diffusion, computing the FP coefficients requires information about the wavenumber power spectrum of magnetic fluctuations. The latter can be inferred from the frequency spectra obtained by Voyager 1 and 2 (Burlaga et al. 2018, 2020; Fraternale et al. 2019). Unfortunately, single-point observations are insufficient to determine the nature of these magnetic fluctuations; the situation is exacerbated by the absence of plasma velocity measurements. Typical wave speeds in the OHS are comparable to the plasma-frame speed of each spacecraft, so the Taylor hypothesis cannot be directly applied. However, the polarization of the fluctuations offers some clues. As already mentioned, while most of the fluctuating power is in the direction perpendicular to $\boldsymbol{B}$, a significant parallel (i.e., compressive) component is also present, which could even dominate the energy balance close to the HP, where the fluctuations are very weak.

It is not known whether the compressive component has a preferred direction of propagation (e.g., away from the HP). If that were the case, one would expect the low-energy particles to become nongyrotropic. Because we would prefer to stay within the framework of nearly gyrotropic diffusive transport, we will assume that the compressive component is axisymmetric with respect to the mean field. The transverse fluctuations observed by Voyager 1 in 2015–2016 can be interpreted as a superposition of Alfvén waves traveling at different angles to the mean field. While in principle all wavevector directions could be present, we restrict the following analysis to a situation where the wavevectors are either parallel or perpendicular to $\boldsymbol{B}$. We therefore postulate that the turbulence in the VLISM consists of three components, Alfvénic (slab), 2D transverse (incompressible), and 2D longitudinal (compressive). The first two types are commonly observed in the solar wind (Bieber et al. 1996), while the last one might be interpreted as an ensemble of fast magnetosonic waves traveling perpendicular to the mean field (however, see Lee & Lee 2020). Compared with fully 3D turbulence, this $2+1$ geometry is much easier to handle analytically.

Consider three reference frames, the plasma frame (PF), the wave frame (WF), and the spacecraft frame (SF), moving with velocities $\boldsymbol{V}_p$, $\boldsymbol{V}_w$, and $\boldsymbol{V}_s$ relative to the fixed (solar) frame, respectively. While all measurements are performed in the SF, modeling cosmic-ray transport requires an expression for the PSD tensor in the WF (or PF), which must be inferred. In dealing with the Voyager observations it is convenient to use the spacecraft/heliographic (also known as RTN) coordinates (Burlaga 1984). We introduce a simplified model geometry where the mean magnetic field is in the T-direction (the measured field is mainly in the T-direction, but has a minor N-component), $\boldsymbol{V}_s$ is in the R-direction, and $\boldsymbol{V}_p$ is in the $-R$-direction (toward the HP), as shown in Figure 1. The last assumption is not well justified because the plasma flow vector almost certainly has a significant tangential component, but its direction is unknown, and to keep the model simple, we choose to ignore it.

Burlaga et al. (2015, 2018, 2020) used daily averaged magnetic field data, so these studies were limited to the frequency range $\omega_{\min} < \omega < \omega_{\max}$ with $\omega_{\min} = 1.5 \times 10^{-7}$ s^{-1} and $\omega_{\max} = 3.6 \times 10^{-5}$ s^{-1}. At the lower end of this frequency range, the spectra of the three magnetic field components were power laws with indices ranging from -1.2 to -2. Because the spectra appear to harden with energy near the high end of the frequency range, frequencies above $\sim 10^{-5}$ s^{-1} were thought to be contaminated by noise. By using 48 s averaged data, Fraternale et al. (2019) extended the power spectrum to frequencies $\sim 6 \times 10^{-4}$ s^{-1} (higher frequencies were also reported, but the resulting PSD

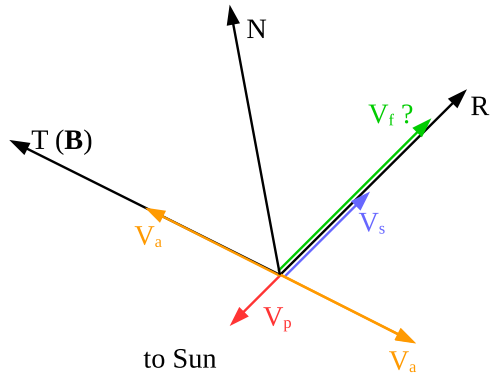

Figure 1. Model plasma, wave, and spacecraft velocity vectors relative to the RTN coordinate system. The spacecraft (Voyager 1 in this case) is traveling in the $+R$-direction with speed $V_s = 17$ km s^{-1}, and the plasma is assumed to flow in the $-R$-direction with speed V_p. Slab fluctuations propagate in the $+T$- and $-T$-directions (along the mean magnetic field) with speed V_a. Transverse 2D fluctuations are convected with the flow, while longitudinal fluctuations can in principle be traveling outward from the HP with speed V_f relative to the plasma.

descended below the instrument noise level of the Voyager magnetometer). The resulting spectra were fitted with power laws with indices between -1.4 and -1.9. The spectra also showed hardening with frequency approaching the power-law index of -1. This result was corroborated by Lee & Lee (2020). The cause of this spectral hardening is unknown (and might be due to noise). Waves generated by the neutral hydrogen pickup process could contribute to the fluctuation level (Florinski et al. 2010, 2016; Liu et al. 2012; Sheng et al. 2021), but in the frequency range above 10^{-3} s^{-1}. In the absence of an explanation, we assume here that the observed PSDs are uninterrupted power laws over the entire frequency range covered by the observations.

For transport purposes, we are interested in the 3D WF wavenumber spectrum $P_{ij}(\boldsymbol{k})$ that is related to the SF frequency-domain power spectrum $P_{\mathrm{obs},ij}(\omega)$ through

$$P_{\mathrm{obs},ij}(\omega) = 2\int_{-\infty}^{\infty} P_{ij}(\boldsymbol{k})\delta \times [\omega - (\boldsymbol{V}_p + \boldsymbol{V}_w - \boldsymbol{V}_s)\cdot\boldsymbol{k}]d^3k. \quad (5)$$

The factor of 2 in front comes from conversion to a one-sided spectrum containing positive frequencies only. Using Equation (5), one can construct a WF model PSD satisfying the SF observations of the frequency spectrum. A difficulty arises because the power spectrum in the VLISM extends down to very small wavenumbers corresponding to very large wavelengths, in principle to parsec scales, if some of the turbulence is of interstellar origin (Haverkorn et al. 2008). The energy range is probably inaccessible to in situ observations given the remaining lifetime of the Voyager mission. Strictly speaking, these very large-scale fluctuations must be treated deterministically rather than statistically because their size exceeds the size of the system under study (~1000 au). Because such information is not available, one might expect that a typical cosmic-ray particle (a proton within the energy range between a few hundred megaelectronvolts and a few gigaelectronvolts) would exhibit superdiffusive behavior relative to the mean magnetic field. Below we will argue that this is indeed the case for the OHS.

3. Theory of Cosmic-Ray Transport for the Three-component Plasma-frame Turbulence Model

3.1. Power Spectra

In this section we present model expressions for the transport coefficients of energetic charged particles in a turbulent environment where most of the spectral power exists on spatial scales much larger than the particle's Larmor radius. Much of the development leading to the final closed form expressions for the FP coefficients has been done elsewhere, and readers interested in the details of the derivations are referred to the cited literature. An exhaustive reference list can be found in the review of the physics of cosmic-ray transport by Engelbrecht et al. (2022).

We assume that magnetic fluctuations in the VLISM are of three distinct types, slab/Alfvénic, with wavevectors parallel to $\boldsymbol{B}$ and $\delta\boldsymbol{B}\perp\boldsymbol{B}$ (index "A"), 2D transverse, interpreted as nonpropagating incompressible structures, with wavevectors orthogonal to $\boldsymbol{B}$ and $\delta\boldsymbol{B}\perp\boldsymbol{B}$ (index "T"), and 2D longitudinal, interpreted as compressive magnetosonic waves traveling normally to the mean field, with wavevectors also orthogonal to $\boldsymbol{B}$ and $\delta\boldsymbol{B}\parallel\boldsymbol{B}$ (index "L"). To avoid confusing the T-component and the T-direction, please remember that, in what follows, the former is only used for upper indices, while the latter is only used for lower indices. All calculations will be performed in field-aligned coordinates, where the unit vector $\hat{\boldsymbol{e}}_z$ is parallel to $\boldsymbol{B}$, $\hat{\boldsymbol{e}}_x$ is a random (owing to axial symmetry) unit vector in the normal plane, and $\hat{\boldsymbol{e}}_y$ completes the right-handed triad. The PSDs of each component in the WF are given by

$$P_{ij}^{A}(\boldsymbol{k}) = \frac{\delta(k_\perp)P^A(k_\parallel)}{4\pi k_\perp}\begin{pmatrix}1&0&0\\0&1&0\\0&0&0\end{pmatrix}, \quad (6)$$

$$P_{ij}^{T}(\boldsymbol{k}) = \frac{\delta(k_\parallel)P^T(k_\perp)}{2\pi k_\perp}\begin{pmatrix}\sin^2\psi & -\sin\psi\cos\psi & 0\\ -\sin\psi\cos\psi & \cos^2\psi & 0\\ 0&0&0\end{pmatrix}, \quad (7)$$

and

$$P_{ij}^{L}(\boldsymbol{k}) = \frac{\delta(k_\parallel)P^L(k_\perp)}{2\pi k_\perp}\begin{pmatrix}0&0&0\\0&0&0\\0&0&1\end{pmatrix}. \quad (8)$$

Here $k_\parallel = k_z$ (i.e., can be negative), $k_\perp = (k_x^2 + k_y^2)^{1/2}$, $\psi = \tan^{-1}(k_y/k_x)$, and the spectral shape functions P^A, P^T, and P^L are defined in such a way that the integral of the trace of the power spectral tensor is equal to the magnetic variance of the respective kind of turbulence. The zero-helicity assumption is evident from the symmetry of the PSD tensors.

The OHS is a region where turbulent fluctuations from multiple sources could in principle coexist. The first is interstellar turbulence driven by supernova explosions and interactions between interstellar clouds. The second is locally produced fluctuations, perhaps as a result of a macroscopic instability at the HP (e.g., Florinski et al. 2005; Borovikov et al. 2008). The third is heliospheric fluctuations transmitted across the HP (Zank et al. 2017). The combined power spectrum from all of these sources might look like that shown in Figure 2. The interstellar spectrum has a Kolmogorov power slope characteristic of fully developed isotropic turbulence down to the outer scale $l_{0,\mathrm{IS}} = 2\pi/k_{0,\mathrm{IS}} \sim 2$–4 pc (Haverkorn et al. 2008), while at

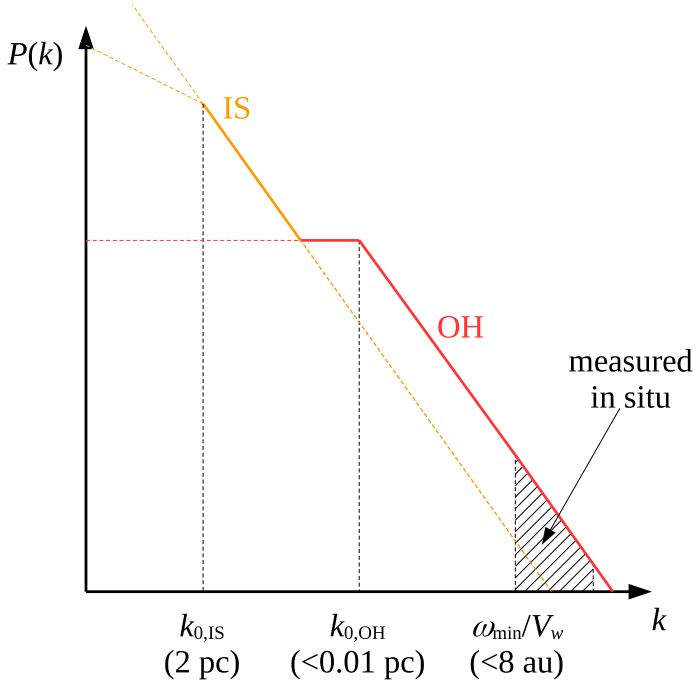

Figure 2. An illustration of the power spectrum of magnetic fluctuations in the OHS. The ISM component (orange) dominates on scales of up to 100 pc, but is much weaker than the locally generated turbulence (red) on scales shorter than 2000 au or 0.01 pc. We assume that the latter has a bend-over (a transition between the energy and inertial ranges) at the wavenumber $k_{0,OH}$ corresponding to a characteristic scale of 0.01 pc. The dissipation range is not shown.

even larger scales, the slope could be shallower (Minter & Spangler 1996); although, this was disputed by Chepurnov & Lazarian (2010). The outer scale of the local component is unknown, but Burlaga et al. (2018) estimated it to be 2000 au or 0.01 pc assuming energy equipartition between the mean and turbulent fields. However, Xu & Li (2022) argued for a shorter outer scale of ∼200 au based on their analysis of turbulence damping by ion-neutral collisions. In any case, for the interstellar component, the inferred intensity of fluctuations in the range of wavenumbers sampled by the Voyagers does not exceed a hundredth of the measured intensity. We can therefore postulate that the ISM turbulence is dominant at parsec scales, but is obscured by turbulence of circumheliospheric origin on scales shorter than $l_{0,OH} = 2\pi/k_{0,OH}$ that will be treated as a free parameter in the model.

We will now focus exclusively on the OHS turbulence and drop the subscript "OH" from all terms. One should, in principle, leave open the possibility that the L-component has a different value of l_0 than the A- and T-components if the former is of heliospheric origin, as proposed in Zank et al. (2017), while the other two are generated in the OHS. However, none of these scales have actually been measured, and to avoid cluttering our simple model with free parameters, we will assume that all three components share the same value of l_0 and the respective k_0. In what follows we will examine a range of values in order to elucidate the role of this parameter in determining the cosmic-ray transport regime. The spectrum will eventually roll over at very small (kinetic) scales, but such small fluctuations affect neither the overall turbulent energy, nor GCR propagation, and we can also take the upper limit to be $k = \infty$.

The characteristic size of the physical system we are investigating is under 1000 au. In this situation, a typical cosmic-ray particle does not sample the entire range of wavenumbers. This means turbulence is not homogeneous, and a statistical description of cosmic-ray transport breaks down. Strictly speaking, one must solve a deterministic problem of transport in a specific realization of the turbulent field as was done in Zirnstein et al. (2020). An alternative is to obtain a representation of the "large-scale" or background magnetic field as best we can, and treat the "short-scale" fluctuations statistically. This scale separation is somewhat artificial, but is often made when studying particle transport in a rapidly varying plasma background (e.g., near a shock wave front). In practical terms, one can ignore the interstellar fluctuations altogether, or consider them a part of the background field. One might hope, in particular, that the large-scale magnetic field structure around the heliosphere will be revealed with the help of the next generation of interstellar explorer missions. We will likewise ignore the energy range of OHS turbulence, if it exists, and assume similar power-law spectra for each component, namely

$$P^A(k_\parallel) = \langle (\delta B^A)^2 \rangle \frac{\gamma - 1}{2k_0} \left(\frac{|k_\parallel|}{k_0} \right)^{-\gamma}, \tag{9}$$

$$P^{T/L}(k_\perp) = \langle (\delta B^{T/L})^2 \rangle \frac{(\gamma - 1)}{k_0} \left(\frac{k_\perp}{k_0} \right)^{-\gamma}, \tag{10}$$

where $\langle (\delta B^A)^2 \rangle$, $\langle (\delta B^T)^2 \rangle$, and $\langle (\delta B^L)^2 \rangle$ are the partial magnetic variances of the Alfvén, transverse and compressible components, respectively, in the spectral range between k_0 and infinity. Note that only a portion of the PSD has been sampled by the Voyagers. The smallest resolved wavenumber is $\sim \omega_{min}/V_w \sim (5\text{–}10) \times 10^{-14}$ cm^{-3}, corresponding to wavelengths between 4 and 8 au, as shown in Figure 2.

3.2. Fokker–Planck Coefficients

The slab contribution to the pitch-angle scattering coefficient $D_{\mu\mu}$ is well known from the conventional quasi-linear theory (QLT). It is produced by a resonant interaction with Alfvén waves, and is given by

$$D^A_{\mu\mu} = \frac{\pi\Omega^2}{2B^2}\frac{1-\mu^2}{v|\mu|}P^A\left(\frac{\Omega}{v\mu}\right) \tag{11}$$

(Jokipii 1966). Equation (11) assumes $V_w/v \ll 1$ and ignores all wave propagation effects, which is a good approximation for gigaelectronvolt protons. Pure slab turbulence only admits variation along the mean field and has two ignorable coordinates, so the particles are tied to the field lines they started on (Jones et al. 1998). Perpendicular transport might look like diffusion on short spatial scales, but eventually reduces to compound diffusion after a sufficient number of scattering (Mace et al. 2000), so $D^A_\perp = 0$.

We now concentrate on the two 2D turbulence components. We use the Bieber et al. (1994) representation of the two-point two-time correlation tensors $R_{ij}(\boldsymbol{\xi},\ \tau) = \langle \delta B_i(\boldsymbol{r},\ t)\delta B_j(\boldsymbol{r}+\boldsymbol{\xi},\ t+\tau)\rangle$, where $\boldsymbol{\xi}$ and τ are the spatial and time lags, respectively, which includes "dynamic decorrelation" effects,

$$R_{ij}(\boldsymbol{\xi},\ \tau) = \int_{-\infty}^{\infty} P_{ij}(\boldsymbol{k})e^{i\boldsymbol{k}\cdot\boldsymbol{\xi}}e^{-\Gamma|\tau|}d^3k, \tag{12}$$

where $\Gamma(\boldsymbol{p},\ \boldsymbol{k})$ describes the time rate of decay of the correlation functions that is interpreted in terms of a dynamic nature of the turbulence or trajectory deviation from the unperturbed helix (Bieber & Matthaeus 1991). The standard approach involves calculating the Lagrangian correlations along the past trajectory of the type

$$\begin{aligned} R_{ij}(-\tau) &= R_{ij}(\boldsymbol{r}(t-\tau) - \boldsymbol{r}(t),\ -\tau) \\ &= \int_{-\infty}^{\infty}\int_0^{\infty}\int_0^{2\pi} k_\perp P_{ij}(\boldsymbol{k})e^{-\Gamma\tau}\sum_{n=-\infty}^{\infty}\sum_{m=-\infty}^{\infty} J_n(\eta)J_m(\eta) \\ &\quad\times\cos[m\Omega\tau + (n-m)(\psi-\varphi)]dk_\parallel dk_\perp d\psi \end{aligned} \tag{13}$$

(e.g., Hall & Sturrock 1967; Schlickeiser & Achatz 1993; le Roux et al. 2004), where φ is the gyrophase angle and

$$\eta = \frac{k_\perp v\sqrt{1-\mu^2}}{\Omega}. \tag{14}$$

Some straightforward, but tedious, calculations then lead to

$$\begin{aligned} D^T_{\mu\mu} &= \frac{\Omega^2(1-\mu^2)}{B^2}\int_0^\infty [\cos\Omega\tau R^T_{xx}(-\tau) - \sin\Omega\tau R^T_{xy}(-\tau)]d\tau \\ &= \frac{2\Omega^2(1-\mu^2)}{B^2}\int_{k_{0,\mathrm{OH}}}^\infty \sum_{n=1}^\infty \frac{\Gamma}{\Gamma^2+n^2\Omega^2}\frac{n^2J_n^2(\eta)}{\eta^2}P^T(k_\perp)dk_\perp, \end{aligned} \tag{15}$$

$$D^L_{\mu\mu} = 0, \tag{16}$$

and

$$\begin{aligned} D_\perp &= \frac{v^2\mu^2}{B^2}\int_0^\infty R^T_{xx}(-\tau)d\tau \\ &\quad + \frac{v^2(1-\mu^2)}{2B_0^2}\int_0^\infty \cos\Omega\tau R^L_{zz}(-\tau)d\tau \\ &= \frac{v^2}{2B^2}\int_{k_{0,\mathrm{OH}}}^\infty \sum_{n=-\infty}^\infty \frac{\Gamma}{\Gamma^2+n^2\Omega^2}\left\{\mu^2J_n^2(\eta)P^T(k_\perp)\right. \\ &\quad \left. + (1-\mu^2)\left[\frac{n^2J_n^2(\eta)}{\eta^2} + J_n{}'^2(\eta)\right]P^L(k_\perp)\right\}dk_\perp. \end{aligned} \tag{17}$$

Note that we tacitly assumed a common value of $k_{0,\mathrm{OH}}$ for the T and L turbulence components. In the QLT limit ($\Gamma = 0$), Expression (15) is reduced to zero, while Equation (17) is infinite (e.g., Shalchi et al. 2004; le Roux & Webb 2007). Physically, this means that the transport is a drift motion, rather than diffusion.

We adopt the decorrelation rate from the weakly nonlinear theory (WNLT), developed by Shalchi et al. (2004), which is given by

$$\Gamma = \frac{2D_{\mu\mu}}{1-\mu^2} + D_\perp k_\perp^2. \tag{18}$$

The first term in Equation (18) is set to zero when computing $D_{\mu\mu}$. The two coupled nonlinear integral equations for $D^T_{\mu\mu}$ and $D_\perp$ can then be solved numerically, but the method is impractical for trajectory integration. A critical simplification can be made if the second term in Equation (18) is much larger than the first (we shall see later that this is indeed the case), so that the coupling between $D_\perp$ and $D^T_{\mu\mu}$ is only one way (the latter depends on the former). Shalchi & Schlickeiser (2004a) found a Padé approximant for the series in Equation (15). Using their result and the power spectrum of Equation (10), the expression for $D^T_{\mu\mu}$ can be reduced to

$$\begin{aligned} D^T_{\mu\mu} &= (1-\mu^2)\frac{\langle(\delta B^T)^2\rangle}{B^2}(\gamma-1)k_0D_\perp\int_{k_0}^\infty \\ &\quad\times\left[\frac{2k_\perp^4D_\perp^2}{\Omega^2} + \frac{k_\perp^2v^2(1-\mu^2)}{\Omega^2} + 2\right]^{-1}\left(\frac{k_\perp}{k_0}\right)^{2-\gamma}dk_\perp. \end{aligned} \tag{19}$$

The integration in Equation (19) can be performed, but an intermediate step using complex math is required that we wish to avoid for practical reasons. Instead, we consider two limits: (1) the case of dominant field-aligned streaming, and (2) the case of dominant perpendicular diffusion. In the first limit, one obtains

$$\begin{aligned} D^T_{\mu\mu,1} &\approx \frac{(1-\mu^2)D_\perp k_0^2}{2(1+\xi_1^2)}\frac{\langle(\delta B^T)^2\rangle}{B^2}{}_2F_1 \\ &\quad\times\left(1,\ 1,\ \frac{\gamma+1}{2};\ \frac{1}{1+\xi_1^2}\right), \end{aligned} \tag{20}$$

where

$$\xi_1 = \frac{vk_0\sqrt{1-\mu^2}}{\sqrt{2}\,\Omega}, \tag{21}$$

while in the second limit

$$D^T_{\mu\mu,2} \approx \frac{(1-\mu^2)D_\perp k_0^2}{2(1+\xi_2^2)}\frac{\gamma-1}{\gamma+1}\frac{\langle(\delta B^T)^2\rangle}{B^2}\,{}_2F_1 \times\left(1,\,1,\,\frac{\gamma+5}{2};\,\frac{1}{1+\xi_2^2}\right), \tag{22}$$

where

$$\xi_2 = \frac{D_\perp k_0^2}{\Omega}. \tag{23}$$

The expression that gives a good approximation for all values of μ and k_0 is

$$D^T_{\mu\mu} \approx \frac{D^T_{\mu\mu,1}D^T_{\mu\mu,2}}{\sqrt{{D^T_{\mu\mu,1}}^2+{D^T_{\mu\mu,2}}^2}}. \tag{24}$$

The series in Equation (17) were discussed by Shalchi & Schlickeiser (2004b), but no unified expression was found that would satisfy all limiting cases. Numerical evaluation reveals that essentially only the lowest-order terms contribute to the integral because of the rapidly decreasing power spectrum, and the approximation $\eta \ll 1$ is valid. Then

$$D_\perp^2 = \frac{v^2\mu^2}{2B^2}\int_{k_0}^\infty \frac{P^{bb,T}(k_\perp)}{k_\perp^2}dk_\perp + \frac{v^4(1-\mu^2)^2}{8B^2\Omega^2}\int_{k_0}^\infty P^{bb,L}(k_\perp)dk_\perp. \tag{25}$$

Using the power spectrum of Equation (10), one obtains

$$D_\perp = v\left[\frac{\gamma-1}{\gamma+1}\frac{\mu^2}{2k_0^2}\frac{\langle(\delta B^T)^2\rangle}{B^2} + \frac{v^2(1-\mu^2)^2}{8\Omega^2}\frac{\langle(\delta B^L)^2\rangle}{B^2}\right]^{1/2}. \tag{26}$$

A similar expression was obtained by le Roux & Webb (2007). Strauss et al. (2016) also arrived at an expression similar to Equation (26) by assuming that $D_\perp \sim l_\perp\langle V_d^2\rangle^{1/2}$, where $l_\perp$ is the perpendicular correlation length, corresponding, approximately, to our k_0^{-1}, and $\langle V_d^2\rangle$ is the ensemble-averaged square of the drift velocity. In that interpretation the transverse 2D turbulence acts through curvature drift; therefore, its contribution to the perpendicular diffusion coefficient has a maximum at $\mu = \pm 1$, while the longitudinal 2D turbulence produces gradient drift, so its contribution maxes out at $\mu = 0$. The latter conveniently reduces the $\mu = 0$ gap in the perpendicular diffusion coefficient and, through the coupling provided by Equation (22), in pitch-angle diffusion as well. Apart from that limit, however, the ratio of the longitudinal to transverse 2D turbulence contributions to $D_\perp$ is proportional to $vk_0/\Omega \ll 1$, so the former component plays only a minor role in perpendicular transport (and no role at all in pitch-angle scattering). It then follows from Equation (26) that the perpendicular diffusion coefficient is directly proportional to the value of the small wavenumber cutoff $k_0 = 2\pi/l_0$. By examining a broad range of values for l_0, from 1000 au down to 1 au, we will show that the situation is actually more complicated, and the actual particle transport regime could deviate from the model's predictions.

4. Evaluation of Fokker–Planck Coefficients Based on Turbulence Observations

We now proceed to estimate the *partial* variances of the three turbulence components in the wavenumber range accessible to Voyager 1. The numerical estimates performed in this section are based on typical values of VLISM parameters measured by Voyagers 1 and 2 (see Section 1). We use a number density $n = 0.1$ cm^{-3} and a mean magnetic field strength $B = 0.5$ nT. These values yield a characteristic Alfv́en speed $V_A \sim 34$ km s^{-1}.

The 3D PSDs for each component are given by Equations (6)–(8), but they can also be expressed in terms of observed parameters, such as the variances $\langle(\delta B^{A/T/L}_{\rm obs})^2\rangle$, the smallest sampling frequency $\omega_{\rm min}$, and the corresponding wavenumbers $k_{\rm min}^{A/T/L}$. Because each type of fluctuation is sampled at a different speed (see Figure 1), the same interval in frequency space is mapped to a different wavenumber range. Alfvénic fluctuations are assumed to have phase velocities $\boldsymbol{V}_w^A = \pm V_A\hat{\boldsymbol{T}}$. This is orthogonal to the spacecraft velocity $\boldsymbol{V}_s = V_s\hat{\boldsymbol{R}}$ and the plasma velocity $\boldsymbol{V}_s = -V_s\hat{\boldsymbol{R}}$ vectors in our simplified model, so the sampling speed is $V_A \sim 34$ km s^{-1}. Assuming the transverse turbulence is frozen into the plasma, we have $\boldsymbol{V}_w^T = 0$, and the sampling speed is $V_p + V_s \sim 27$ km s^{-1}, taking a plausible value of $V_p = 10$ km s^{-1}. We consider two possibilities for the longitudinal fluctuations. The first is that they are convected with the plasma, in which case their sampling speed is the same as for the transverse component. The second is that they travel outward from the HP with speed $\boldsymbol{V}_w^L = V_f\hat{\boldsymbol{R}}$ (in the PF), where $V_f = \sqrt{V_A^2 + C_s^2}$, C_s, being the adiabatic sound speed, is the fast magnetosonic speed. In the latter case, the sampling speed becomes $V_f - V_p - V_s \sim 17$ km s^{-1}. Strictly speaking, the fluctuations are not axially symmetric in the second model, but the difference should be of the order of $V_f/v \ll 1$.

Applying the sampling operator of Equation (5) to the WF power spectra of Equations (9) and (10) yields the following nonzero components of the SF frequency PSD tensor:

$$P^A_{{\rm obs},RR} = P^A_{{\rm obs},NN} = \frac{(\gamma-1)\langle(\delta B^A_{\rm obs})^2\rangle}{\omega_{\rm min}}\frac{1}{2}\left(\frac{\omega}{\omega_{\rm min}}\right)^{-\gamma}, \tag{27}$$

$$P^T_{{\rm obs},RR} = \frac{P^T_{{\rm obs},NN}}{\gamma} = \frac{(\gamma-1)\langle(\delta B^T_{\rm obs})^2\rangle}{\omega_{\rm min}}\frac{\Gamma(\gamma/2)}{2\sqrt{\pi}\,\Gamma[(\gamma+3)/2]}\left(\frac{\omega}{\omega_{\rm min}}\right)^{-\gamma}, \tag{28}$$

$$P^L_{{\rm obs},TT} = \frac{(\gamma-1)\langle(\delta B^L_{\rm obs})^2\rangle}{\omega_{\rm min}}\frac{\Gamma(\gamma/2)}{\sqrt{\pi}\,\Gamma[(\gamma+1)/2]}\left(\frac{\omega}{\omega_{\rm min}}\right)^{-\gamma}. \tag{29}$$

The corresponding smallest wavenumbers for the first model for the L fluctuations are

$$k^A_{\rm min} = \frac{\omega_{\rm min}}{|V_A|} = 4.4\times10^{-14}\,{\rm cm}^{-1},$$
$$k^{T/L}_{\rm min} = \frac{\omega_{\rm min}}{|V_s - V_p|} = 6.3\times10^{-14}\,{\rm cm}^{-1}. \tag{30}$$

while for the second model, we have

$$k_{\min}^{L} = \frac{\omega_{\min}}{|V_f - V_s - V_p|} = 8.8 \times 10^{-14}\ \mathrm{cm}^{-1}. \quad (31)$$

For V1 Interval 1, the variance in the frequency range studied in Burlaga et al. (2015) was $\sim 2.2 \times 10^{-4}$ nT^2 with the eigenvalues of the covariance matrix $\langle \delta B_{RR}^2 \rangle$, $\langle \delta B_{TT}^2 \rangle$, and $\langle \delta B_{NN}^2 \rangle$ comprising 17%, 47%, and 36% of the total, respectively. Fraternale et al. (2019) reported a somewhat larger value of the total variance at 2.4×10^{-4} nT^2 in their wider frequency range. V1 Interval 2 values are probably more representative of the VLISM in general, so in what follows we mostly rely on that interval as the reference (V1 Interval 3 has similar properties to V1 Interval 2). During the second interval, the measured variance was larger at nearly 3.6×10^{-4} nT^2 with the three components comprising 32%, 21%, and 47% of the total, respectively (Burlaga et al. 2018). The T-component has not changed appreciably, while the R- and N-components were enhanced by a factor of >2 compared with the first interval.

Integration of Equations (27)–(29) over the measured frequencies yields the following linear system for the Eulerian variances:

$$\begin{pmatrix} 0.5 & 0.26 & 0 \\ 0 & 0 & 0.71 \\ 0.5 & 0.45 & 0 \end{pmatrix} \begin{pmatrix} \langle (\delta B_{\rm obs}^{A})^2 \rangle \\ \langle (\delta B_{\rm obs}^{T})^2 \rangle \\ \langle (\delta B_{\rm obs}^{L})^2 \rangle \end{pmatrix} = \begin{pmatrix} \langle \delta B_{{\rm obs},RR}^2 \rangle \\ \langle \delta B_{{\rm obs},TT}^2 \rangle \\ \langle \delta B_{{\rm obs},NN}^2 \rangle \end{pmatrix} \quad (32)$$

with the solutions $(\langle (\delta B_{\rm obs}^{A})^2 \rangle, \langle (\delta B_{\rm obs}^{T})^2 \rangle, \langle (\delta B_{\rm obs}^{L})^2 \rangle) = (0.4, 2.2, 1.45) \times 10^{-4}$ nT^2 and $(0.91, 3.16, 1.18) \times 10^{-4}$ nT^2 for the two intervals, respectively. This result overestimates the Alfvénic component that has the fastest sampling speed and (possibly) underestimates the longitudinal component because its sampling speed is the lowest. To provide an equal basis for comparison, we adjust all variances to a single value of $k_{\min} = k_{\min}^{T}$ for all three components and compare the power only in fluctuations with larger wavenumbers. That way, we obtain $(\langle (\delta B_{\rm obs}^{A})^2 \rangle, \langle (\delta B_{\rm obs}^{T})^2 \rangle, \langle (\delta B_{\rm obs}^{L})^2 \rangle) = (0.32, 2.2, 1.45) \times 10^{-4}$ nT^2 for V1 Interval 1 and $(0.72, 3.16, 1.18) \times 10^{-4}$ nT^2 for V1 Interval 2 in the "frozen-in" model of L turbulence. In the fast magnetosonic model, the ratios become $(0.32, 2.2, 1.81) \times 10^{-4}$ nT^2 for V1 Interval 1 and $(0.72, 3.16, 1.47) \times 10^{-4}$ nT^2, respectively. This yields the following WF power ratios for the two periods: 8%/14% slab, 55%/63% transverse 2D, and 37%/23% compressive in the frozen-in model and 8%/14% slab, 52%/59% transverse 2D, and 43%/27% compressive in the magnetosonic model. Note that according to these calculations, the total WF turbulent power increased by only 27% from the first to the second interval, while the observed SF power rose by 62%. This discrepancy is due to (a) the difference in weights with which each turbulence component contributes to the power measured in the SF, and (b) the difference in the sampling speeds. The compressive component declined by less than 20% in the V1 Interval 2, which can be explained by an increase in the plasma velocity of only 4 km s^{-1}. Such an increase is expected because the VLISM flow decelerates on approach to the HP (e.g., Usmanov et al. 2016).

Guided by V1 Interval 2 values, we assume the power of the A, T, and L components to be 10:60:30 percent of the total, respectively. The measured and modeled frequency spectra for Interval 2 are compared in Figure 3. They have the same power in the frequency range between $\omega_{\min}$ and $\omega_{\max}$. It should be remembered that the model spectra are estimates based on a number of simplifying assumptions, the most severe of which are the identification of the *T*-direction as the direction of the mean magnetic field and the assumption of the same power-law index for all three components. A more careful analysis could be performed in the spirit of Fraternale et al. (2019), who projected the magnetic field vector onto the actual measured magnetic field direction (that has a measurable *N*-component) and reported separate power-law indices for each component. However, such a detailed analysis is beyond the scope of this paper. Note that the model spectra are below the measured values at high frequencies. This is not necessarily a problem because the latter are likely affected by the instrument noise and only give the upper limits on the actual power spectra (Burlaga et al. 2018).

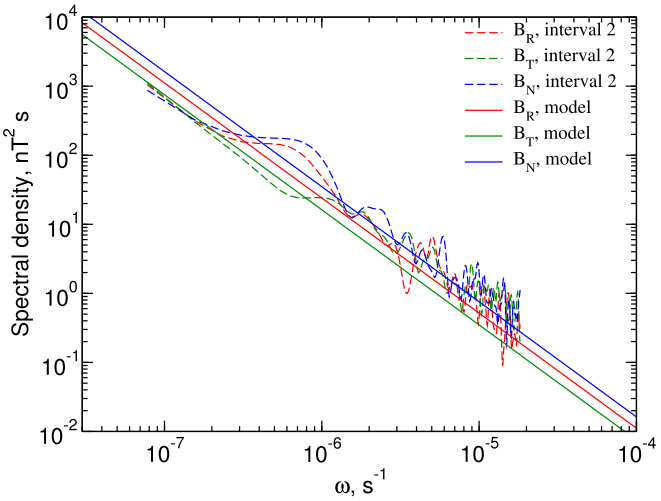

Figure 3. Voyager 1 measured frequency spectral densities in each of the three components during V1 Interval 2, and the corresponding model frequency spectra given by Equations (27)–(29).

Figure 4 plots the theoretical pitch-angle and the perpendicular diffusion coefficients for a 1 GeV proton in a 0.5 nT magnetic field and model VLISM turbulence conditions for three values of l_0 from 1–100 au. For small-scale turbulence, the perpendicular diffusion coefficient is much flatter (and will eventually peak at $\mu = 0$), but such scales are not realistic given the size of the heliosphere. Strauss et al. (2016) proposed an inverted profile for $D_\perp$ that peaked at $\mu = 0$ to explain the difference in behavior between streaming and gyrating ions just beyond the HP. For this to work, a sub-astronomical unit value for k_0^{-1} is required, which is completely unrealistic for the VLISM, where much larger fluctuations have been measured, but could in principle, hold within the HP transition layer whose thickness is of the order of 1 au (Burlaga & Ness 2009b; Krimigis et al. 2019).

The slab component provides weak scattering, especially near 90° (dashed blue line). Adding the 2D component increases the scattering rate in the model by more than an order of magnitude and mostly eliminates the resonance gap (solid blue line). The possible flattening of the spectral slope suggested by Fraternale et al. (2019) would result in more rapid scattering at small values of μ. Pitch-angle scattering in the VLISM is still very slow compared with typical scattering rates in the solar wind, which is to be expected based on the very low fluctuation power in the

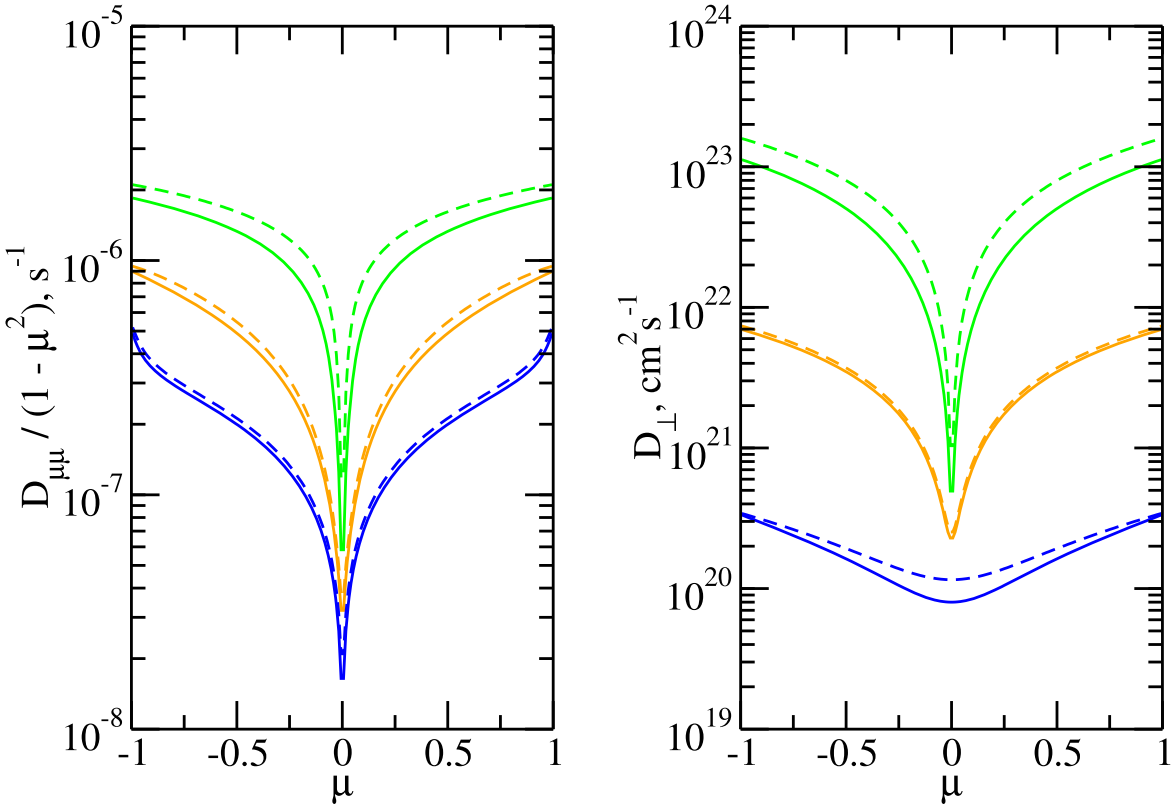

Figure 4. Pitch-angle scattering coefficient $D_{\mu\mu}$ (left) and perpendicular diffusion coefficient D_{xx} as functions of pitch angle for 1 GeV protons using the smallest wavenumber k_0 values of $2\pi/1$ au (blue), $2\pi/10$ au (orange), and $2\pi/100$ au (green). The energies in the Alfvén, transverse, and longitudinal components are 10%, 60%, and 30%, respectively. Solid lines are full numerical solutions to the integral Equations (15) and (17), and dashed lines are the approximate results given by Equations (24) and (26). In both cases, the slab contribution to $D_{\mu\mu}$ was evaluated using Expression (11).

relevant wavenumber range. For an isotropic distribution, the parallel diffusion coefficient of a 1 GeV proton computed from Figure 4 for $l_0 = 100$ au is 1.5×10^{26} cm^2 s^{-1}, which corresponds to the MFP of 1000 au. This is significantly smaller than the MFP used in the LISM modulation studies of Strauss et al. (2013) and Luo et al. (2016), although Guo & Florinski (2014) explored both larger and smaller values.

The gap is also present in $D_\perp$ (green and orange lines in Figure 4), which means that the compressive component is not efficient in transporting particles across the field in the VLISM. This happens because the ratio of the contributions from the L and T modes from Equation (26) is $(\sim r_L k_0)^2 \ll 1$, where r_L is the Larmor radius. Both components' contributions to $D_\perp$ are nonresonant, but the transverse component acts mainly through the small k end of the spectrum. While the compressive component is significant close to the HP, even a small amount of transverse fluctuations will ensure that $D_\perp$ has a minimum at $\mu = 0$. One might argue that the result is contingent on the value of k_0 used in the model. However, even in the most extreme (and unrealistic) situation where $k_0 = \omega_{\min}/V_A$, i.e., there is zero spectral power at frequencies below those sampled by Voyager, the product $r_L k_0$ is still considerably smaller than 1, so the earlier conclusion that compressive turbulence has only a small effect on particle diffusion (Section 3) remains in force.

5. Comparison with Particle Simulations for Homogeneous Turbulence

To support (or refute) the theoretical results derived in the previous sections, we performed a series of particle orbit simulations in homogeneous turbulence. Such a verification is particularly important because the analytic results were derived under a restrictive assumption of diffusive transport, where as both sub- and superdiffusive behavior might be expected for certain turbulent background. Following the well-established methodology (Giacalone & Jokipii 1994; Mace et al. 2000; Tautz & Dosch 2013), a computer simulation integrates a large number of particle trajectories in a prescribed static magnetic field background consisting of a superposition of plane waves with different wavevectors whose amplitudes are distributed according to the prescribed PSD, while their directions and phases are picked at random from the parameter space appropriate for the respective turbulence geometry. For each turbulence component, we defined the shortest and the longest wavelengths ($\lambda_{\min}$ and $\lambda_{\max}$) and divided the corresponding wavenumber interval into N wave modes spaced logarithmically (i.e., the distance between the modes $\Delta k \sim k$). In all numerical experiments reported here, we used 319 field realizations (equal to the number of worker processes). The simulations were run for $t_{\rm sim} \sim 30{,}000\ \Omega^{-1}$, with each particle starting from a randomly picked spatial position with a random initial pitch angle and gyrophase.

All computer simulations reported here used the transport framework of the Space Plasma and Energetic Charged particle TRansport on Unstructured Meshes (SPECTRUM) code capable of integrating large numbers of phase space trajectories based on different transport physics (e.g., Newton–Lorentz, guiding-center, focused transport, isotropic Parker, etc.) and binning the outcome across a multidimensional parameter space at the start, termination, or at recurring checkpoints of

each trajectory. SPECTRUM is written in modern C++, supports parallel execution, and provides a uniform and consistent user interface to the simulation building blocks such as transport physics, plasma background, initial and boundary conditions, and distribution accumulators. The software used in this work was composed of the "Lorentz" trajectory module with a deterministic fifth-order adaptive step integrator of the Dormand–Prince type, the "Waves" background module, the "MomentumShell" initial momentum distribution module, the "TimeRecurrent" time boundary condition module, and the "PositionCumulativeOrder1" and "PositionCumulativeOrder2" binned distribution modules. As the name implies, the latter collects the moments $\langle x_i \rangle$ and $\langle x_i\, x_j \rangle$. The running diffusion coefficient tensor is calculated during post-processing as the central second moment

$$\boldsymbol{\kappa} = \frac{1}{2}\frac{d(\langle \boldsymbol{rr} \rangle - \langle \boldsymbol{r} \rangle \langle \boldsymbol{r} \rangle)}{dt}, \tag{33}$$

where the mean $\langle \boldsymbol{r} \rangle$ is typically very close to zero.

This section also addresses the question of whether charged particle transport in the OHS is drastically different from that in the inner heliosphere even under extremely quiet conditions in the latter case. Giacalone & Jokipii (1999, hereafter GJ1999) previously investigated particle diffusion in the weak turbulence case (their Run 8). In this section we revisit their work and compare the results with the theory of Section 3. We then proceed to simulate transport in the three-component turbulence in the VLISM. Because of the difference in spatial scales between the two environments, we use lower-energy protons in the solar-wind case (31.6 MeV); however, the ratio between the shortest wave in the simulation box and the Larmor radius of the particle is identical in the two environments. The main difference was in the behavior of the magnetic power spectrum at small wavenumbers. For the solar-wind, it had an energy-containing range below the correlation scale of 0.01 au, while the VLISM spectrum was an uninterrupted power law.

5.1. Revisiting Run 8 of GJ1999

Run 8 was the case of weak turbulence with $\langle \delta B^2 \rangle / B^2 = 0.0316$ that most closely approximates the VLISM conditions out of all of the cases examined in GJ1999. The power was partitioned in the 20%–80% ratio between the slab and 2D (transverse-only) components, which is a typical value in the solar wind (Bieber et al. 1996). The other parameters could be found in Table 1 of GJ1999. The spectral shape function of the slab component $P^A(k_\parallel)$ consisted of the small $k_\parallel$ flat energy range and the large $k_\parallel$ inertial range characterized by the $-5/3$ power law. The transverse component spectral function $P^T(k_\perp)$ had the same power law in the inertial range, but was proportional to $k_\perp$ in the energy range. Note that some workers prefer a different spectral shape in the energy range for the 2D component; for example, Matthaeus et al. (2007) had $P^T(k_\perp) \sim$ const, i.e., the amount of spectral power in any annular region of constant width $\Delta k_\perp$ was independent of the wavenumber. Wave modes were logarithmically distributed between $\lambda_{\min} = 10^{-4}$ au and $\lambda_{\max} = 1$ au. Test particles were protons with an energy of 31.6 MeV. A total of 100,000 particles were injected and their trajectories integrated for $t_{\rm sim} = 12$ hr.

The simulations reported here used the "on-the-fly" approach to generate the magnetic field by summing up all of the harmonics at the "current" position of the particle (including the substeps of the Runge–Kutta integrator). This is time consuming, but requires relatively little computer memory. An alternative approach, used by Mace et al. (2000) and Qin et al. (2006), is to pre-compute the field on a very fine numerical grid and use linear interpolation to the particle's position. The main drawback of the "on-the-fly" method is that the simulation runtime is directly proportional to the number of wave modes, which therefore cannot be very large (typically less than a few thousand). Because scattering on slab fluctuations is a resonant process (for weak fluctuations), it is desirable that there should always be a wave resonating with the particle for any value of the pitch angle, or else the strength of the wave–particle interaction could be underestimated. Grid-based models generate a very large number of modes (typically in the millions), and therefore have an advantage in that particular case. Conversely, a particle can interact with the entire broadband spectrum of 2D fluctuations, and therefore a close matching between the wave and particle is not required. We have verified this by performing several runs with only the transverse turbulence component and the number of wave modes varying between 300 and 1500; the results for the perpendicular diffusion were indeed very similar, and in what follows, we use $N^T = 500$. However, slab-only simulations revealed that $\kappa_\parallel$ does depend on the number of wave modes. For this reason, in what follows, we always use the highest number of modes, $N^A = 1500$, for the slab component. The advantages of the "on-the-fly" model are its precision (the field is generated exactly instead of interpolated) and a lack of restriction imposed by the finite box size.

We performed three numerical experiments for the slab-only, 2D-only, and composite turbulence scenarios. The results are summarized in Figure 5, which also plots the theoretical values for comparison. The theoretical diffusion coefficients were computed from the full expressions for $D_{\mu\mu}$ and $D_\perp$ using Equations (3) and (4). The slab-only simulation reached a value of $\kappa_\parallel$ that is fairly close to the QLT prediction, as expected for weak turbulence (the result is not shown, but it is almost exactly the same as in the composite case). Perpendicular transport was not diffusive in this case because the particles were tied to the field line they started on; this effect was discussed elsewhere (Jokipii et al. 1993; Jones et al. 1998). In the transverse-only simulation, parallel transport was essentially scatter-free as can be seen from the continuously increasing value of the running diffusion coefficient. This result is consistent with the QLT that predicts zero scattering from 2D turbulence (see Section 3.2). Qin et al. (2006) also arrived at the same conclusion for the weak turbulence case. On the other hand, WNLT predicts a finite value of the scattering coefficient, which contradicts the numerical result.

For perpendicular diffusion, the numerical values are very close to the theory predictions, but the transport is not strictly diffusive ($\kappa_\perp$ is seen to be slowly decreasing with time). For pure 2D turbulence, this is an expected result because in that case, field lines form closed loops when projected onto the plane normal to the mean field. The particle can diffuse inside the "magnetic island" it was injected into, but not break away from it, so its transport on large timescales is subdiffusive. What is surprising is that $\kappa_\perp$ behaves in a similar manner in the presence of a slab component. Here one would expect that trapping does not take place because slab fluctuations enable field-line meandering. WNLT also predicts an increase in the scattering rate for the composite turbulence compared with the

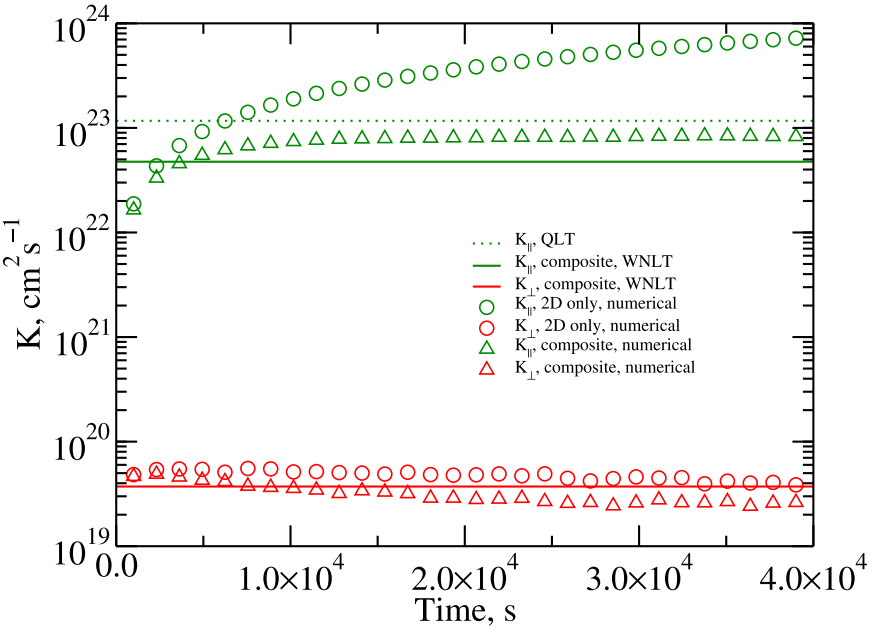

Figure 5. Parallel (green) and perpendicular (red) running diffusion coefficients as a function of time for the GJ1999 Run 8 conditions. Solid lines are theoretical values for composite turbulence based on WNLT equations (Section 3.2), while the dotted line is the slab-only QLT result. Numerical results are plotted with symbols: circles are for the 2D-only case, and triangles are for the composite case. Numerical results for the slab-only simulation are not shown because $\kappa_\parallel$ was very close the composite result, while perpendicular transport was subdiffusive.

slab-only case. The numerical result contradicts the theory, showing virtually no change in the value of $\kappa_\parallel$ from the addition of the transverse turbulence component. Based on these result, it appears that, for the set of parameters used in this experiment, parallel diffusion is best described using standard QLT, while perpendicular diffusion follows the WNLT prescription.

Note that the values of $\kappa_\parallel$ and $\kappa_\perp$ derived for the composite turbulence are significantly larger than those reported in GJ1999. At present we are unable to account for this discrepancy, but note that GJ1999 used a different technique to calculate the diffusion coefficients based on an a priori assumption of diffusive transport as well as fewer wave modes ($N = 185$) than in this work.

5.2. Results for the Inferred VLISM Conditions

For the VLISM, we used $B_0 = 0.5$ nT, $\lambda_{\min} = 0.005$ au, and two values for $\lambda_{\max} = l_0$, 100 au and 1000 au. Only the case of composite turbulence was examined. The power spectrum for each component only had the inertial power-law range and partitioned between the A, T, and L modes in the 10:60:30 percent ratio (see Section 4). The total power was normalized such that it matched the observations in the range of wavenumbers sampled by Voyager 1. The ratio $\langle \delta B^2 \rangle / B^2$ was 0.01 for $l_0 = 100$ au and 0.045 for $l_0 = 1000$ au. Test particles were 1 GeV protons, and the trajectories were integrated for $t_{\rm sim} = 20$ days. Because each trajectory takes considerably longer to integrate than in the solar-wind case, the total number of trajectories was reduced to 50,000. We used 1500 wave modes for the A, 500 for the T, and 200 for the L turbulence components.

The results are shown in Figure 6. Note that the simulation time was not long enough to establish a diffusive regime along the mean magnetic field. The running diffusion coefficient increased through the WNLT predicted values with barely a deviation from linear (ballistic) transport at the end of the run. Increasing l_0 had virtually no effect on $\kappa_\parallel$, again in contradiction with the theory that predicted more scattering in that case. A 1 GeV proton can travel a distance roughly 10 times the size of the heliosphere in 20 days, so in most cases, GCR transport can be described as scatter-free. It is possible, however, that particles confined in a magnetic trap would still experience some scattering.

The behavior of the perpendicular diffusion coefficient is particularly interesting. For $l_0 = 100$ au, its value is very close to the WNLT prediction and shows weakly subdiffusive behavior at later times, similar to the solar-wind case. However, for $l_0 = 1000$ au the transport is superdiffusive on the timescale of the simulation. This is evidently a result of particles effectively interacting with larger and larger fluctuations as time goes by. The superdiffusive regime is new and is quite distinct from the typical diffusive behavior in the solar wind. By the end of the simulation, the $\kappa_\perp$ curve is nearly flat, and a diffusive regime appears to be established with a coefficient some three times greater than theoretical. It is, however, possible that trapping on even larger scales would eventually lead to subdiffusion.

6. Discussion and Conclusions

This work presents an attempt to systematize the observations of turbulent fluctuations in the OHS and use them to infer the transport regime of cosmic rays in the region of interstellar space surrounding the solar system. Despite large uncertainties in the geometry of the turbulence, a simple model was constructed incorporating only the information about the variances and the power spectral slopes. The model used three turbulence components (as opposed to the slab-2D combination often used to describe solar-wind turbulence), where the third component consists of compressive fluctuations. In this context, the word "compressive" means that the fluctuating magnetic field is parallel to the mean field, and not that it contains density fluctuations. However, both could be true if

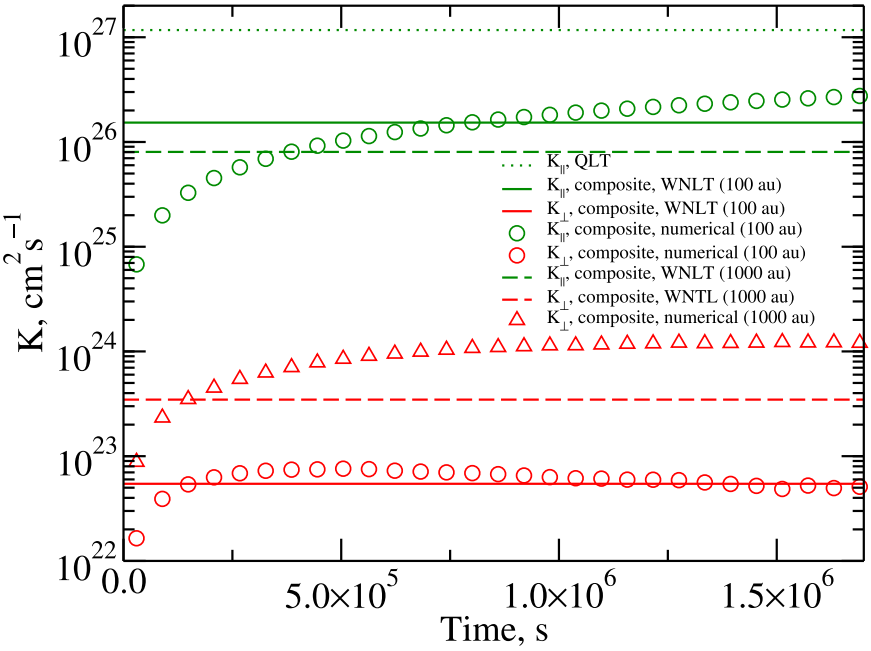

Figure 6. Parallel (green) and perpendicular (red) running diffusion coefficients as a function of time for the VLISM conditions. Solid and dashed lines are theoretical values for composite turbulence for $l_0 = 100$ au and 1000 au, respectively, while the dotted line is the slab-only QLT result. Circles show numerical results for $l_0 = 100$ au. The parallel diffusion coefficient in the $l_0 = 1000$ au case was nearly identical to that for the 100 au case, and is not shown; the corresponding perpendicular diffusion coefficient is shown with triangle symbols.

the compressive fluctuations are interpreted as magnetosonic waves propagating at large angles to the mean magnetic field.

The Taylor hypothesis does not apply in the OHS, and each of the three components can be, in principle, sampled at different speeds, depending on the direction of propagation. This means that the variances measured by the spacecraft are biased, and do not necessarily provide a correct estimate of the fluctuation energy partition ratios between the components. Alfvén waves travel at high speed and large angles to the spacecraft velocity and the plasma flow vectors, and are sampled at relatively high rates, incurring a positive intensity bias. Nonpropagating structures have a smaller SF speed, and so are sampled at somewhat larger wavenumbers than the Alfvén waves. Magnetosonic waves, if propagating away from the HP, are traveling in the same direction as the Voyagers, which therefore measure even shorter fluctuations belonging to this component. The sampling speed depends on multiple factors such as the direction of the mean magnetic field and the magnitude and direction of the plasma flow velocity vector, all of which are expected to vary with distance from the HP. Observations that are several years (and multiple astronomical unit) apart would yield different observables even if the WF turbulence properties did not change at all. For this reason, we recommend caution when interpreting apparent changes in the nature of the turbulence with heliocentric distance.

Turbulent fluctuations in the VLISM are very weak by heliospheric standards. However, weak MHD turbulence is expected to have a softer spectral slope than the observed Kolmogorov-like value (Galtier 2018). The inertial spectral range probably extends to scales of up to ~200–2000 au, where the fluctuations are stronger. If this is the case, we predict superdiffusive transport on timescales of less than several days. Most of the previous work on cosmic-ray transport in the VLISM assumed diffusion both along and across the magnetic field (Strauss et al. 2013; Guo & Florinski 2014; Luo et al. 2016). While this is probably acceptable when modeling large-scale phenomena, cosmic ray transport at the HP or near shock waves might need to be reexamined in light of the new findings. In addition, one would expect enhanced scattering rates due to extra turbulence produced by instabilities associated with shocks and other coherent structures.

If we wish to stay within the limits of diffusive transport, then several practical recommendations could be made. It appears that WNLT provides a fairly accurate description of the perpendicular diffusion process in the VLISM, and Equation (26) is a useful formula for transport work. Typical values of $\kappa_\perp$ are 10^{22}–10^{24} for particles with energies between hundreds of megaelectronvolts to a few gigaelectronvolts. On the other hand, WNLT overpredicts the scattering rate by transverse turbulence, and QLT values computed for only the slab component should be used instead. The parallel diffusion coefficient is probably close to 10^{27} cm^2 s^{-1} at 1 GeV, which corresponds to a parallel MFP of some 10^4 au. This in turn yields $\kappa_\perp/\kappa_\parallel \sim 10^{-4}$–$10^{-5}$.

We acknowledge that the model presented here is limited by the absence of oblique fluctuations that could have additional transport effects due to magnetic trapping (Schlickeiser & Miller 1998). This could be modeled by adding an isotropic turbulence component to the mix. We point out, however, that the effect of trapping is noticeable only for particles with pitch angles near 90°. Giacalone & Jokipii (1999) compared particle diffusion in isotropic and composite (A+T) turbulence using orbit simulations and found little difference in parallel diffusion coefficients between the two, although the perpendicular diffusion coefficient was smaller in the isotropic case by a factor of ~3. The isotropic component, if it exists in the VLISM, would constitute perhaps half of the total turbulent energy, so one might expect that the perpendicular diffusion coefficient would be smaller by a factor of <2 compared with

our results, which is not very significant (but might be worth investigating in a follow-up work).

The long MFPs of GCRs inferred from the model imply that there should be no measurable modulation in the VLISM on average. The values we obtained are similar to those used in computer simulations of Guo & Florinski (2014; specifically, their cases S2 and S4), who calculated constant intensity throughout the VLISM. If Voyager 1 observations are typical of the VLISM, then the parallel diffusion coefficient should decrease and the perpendicular diffusion coefficient should increase with distance from the HP, at least out to 20 au. This is a consequence of the measured increase in turbulence levels in general, and in the transverse component in particular, which is the most efficient in enabling perpendicular diffusion out of all three components.

It is also worthwhile to mention that the low scattering rates obtained in this paper are generally in agreement with the long duration (of the order of 1 yr) of cosmic-ray anisotropy events (Rankin et al. 2019). Current models, based on the idea of particle trapping in the post-shock region (Kóta & Jokipii 2017; Zhang & Pogorelov 2020) also used a very small $D_{\mu\mu}$ or no scattering at all. However, these models also had a very small (or nonexistent) coefficient of cross-field diffusion, which is contrary to our results for $D_{\perp}$. It is possible that stronger cross-field diffusion could facilitate particle escape from the magnetic trap behind the shock wave, but it is not clear how much of an effect it would have without performing detailed modeling of the process.

In a follow-up paper (in preparation), we use the present results to study cosmic-ray propagation around the heliosphere, including and with a particular emphasis on the region of weak magnetic field near the so-called "null point" where the magnetic field is normal to the surface of the HP that is clearly identifiable in numerical MHD models of the global heliosphere (Chalov et al. 2010; Izmodenov & Alexashov 2020). A magnetic trap develops around the null point, where cosmic-ray particles could be stored for an extended period of time. We also examine the cosmic-ray heliosphere access pattern to identify possible weak spots on the HP boundary. The boundary partially shields the rest of the solar system from GCRs, and the new work will help quantify the degree of radiation protection it provides.

This research was supported by NASA grants 80NSSC18K1209, 80NSSC20K0786, 80NSSC20K0603, and Our Heliospheric Shield NASA DRIVE center (grant 80NSSC22M0164).

ORCID iDs

V. Florinski https://orcid.org/0000-0001-5485-2872
J. G. Alonso Guzman https://orcid.org/0000-0001-9581-3167
J. Giacalone https://orcid.org/0000-0002-0850-4233
J. A. le Roux https://orcid.org/0000-0001-9199-2890
M. Opher https://orcid.org/0000-0002-8767-8273

References

Armstrong, J. W., Rickett, B. J., & Spangler, S. R. 1995, ApJ, 443, 209
Baranov, V. B., Krasnobaev, K. V., & Ruderman, M. S. 1976, Ap&SS, 41, 481
Bieber, J. W., & Matthaeus, W. H. 1991, ICRC (Dublin), 3, 248
Bieber, J. W., Matthaeus, W. H., Smith, C. W., et al. 1994, ApJ, 420, 294
Bieber, J. W., Wanner, W., & Matthaeus, W. H. 1996, JGR, 101, 2511
Borovikov, S. N., Pogorelov, N. V., Zank, G. P., & Kryukov, I. A. 2008, ApJ, 682, 1404
Burlaga, L. F. 1984, SSRv, 39, 255
Burlaga, L. F., Florinski, V., & Ness, N. F. 2015, ApJL, 804, L31
Burlaga, L. F., Florinski, V., & Ness, N. F. 2018, ApJ, 854, 20
Burlaga, L. F., & Ness, N. F. 2009a, ApJ, 703, 311
Burlaga, L. F., & Ness, N. F. 2009b, ApJ, 784, 146
Burlaga, L. F., & Ness, N. F. 2016, ApJ, 829, 134
Burlaga, L. F., Ness, N. F., Berdichevsky, D. B., et al. 2020, AJ, 160, 40
Burlaga, L. F., Ness, N. F., Berdichevsky, D. B., et al. 2022, ApJ, 932, 59
Chalov, S. V., Alexashov, D. B., McComas, D. J., et al. 2010, ApJL, 716, L99
Chepurnov, A., & Lazarian, A. 2010, ApJ, 710, 853
Cummings, A. C., Stone, E. C., Heikkila, B. C., et al. 2016, ApJ, 831, 18
Engelbrecht, N. E., Effenberger, F., Florinski, V., et al. 2022, SSRv, 218, 33
Florinski, V., Heerikhuisen, J., Niemiec, J., & Ernst, A. 2016, ApJ, 826, 197
Florinski, V., Jokipii, J. R., Alouani-Bibi, F., & le Roux, J. A. 2013, ApJL, 776, L37
Florinski, V., Stone, E. C., Cummings, A. C., & le Roux, J. A. 2015, ApJ, 803, 47
Florinski, V., Zank, G. P., Heerikhuisen, J., et al. 2010, ApJ, 719, 1097
Florinski, V., Zank, G. P., & Pogorelov, N. V. 2005, JGR, 110, A07104
Fosalba, P., Lazarian, A., Prunet, S., & Tauber, J. A. 2002, ApJ, 564, 762
Fraternale, F., & Pogorelov, N. V. 2021, ApJ, 906, 75
Fraternale, F., Pogorelov, N. V., Richardson, J. D., & Tordella, D. 2019, ApJ, 872, 40
Frisch, P. C. 2007, SSRv, 130, 355
Galtier, S. 2018, JPhA, 51, 293001
Giacalone, J., & Jokipii, J. R. 1994, ApJL, 430, L137
Giacalone, J., & Jokipii, J. R. 1999, ApJ, 520, 204
Goldstein, M. L., Roberts, D. A., & Matthaeus, W. H. 1995, ARA&A, 33, 283
Guo, X., & Florinski, V. 2014, ApJ, 793, 18
Gurnett, D. A., & Kurth, W. S. 2019, NatAs, 3, 1024
Gurnett, D. A., Kurth, W. S., Burlaga, L. F., & Ness, N. F. 2013, Sci, 341, 1489
Gurnett, D. A., Kurth, W. S., & Stone, E. C. 2015, ApJ, 809, 121
Hall, D. E., & Sturrock, P. A. 1967, PhFl, 10, 2620
Haverkorn, M., Brown, J. C., Gaensler, B. M., & McClure-Griffiths, N. M. 2008, ApJ, 680, 362
Izmodenov, V. V., & Alexashov, D. B. 2020, A&A, 633, L12
Jokipii, J. R. 1966, ApJ, 146, 480
Jokipii, J. R., Kóta, J., & Giacalone, J. 1993, GeoRL, 20, 1759
Jones, F. C., Jokipii, J. R., & Baring, M. G. 1998, ApJ, 509, 238
Kóta, J., & Jokipii, J. R. 2000, ApJ, 531, 1067
Kóta, J., & Jokipii, J. R. 2017, ApJ, 839, 126
Krimigis, S. M., Decker, R. B., Roelof, E. C., et al. 2013, Sci, 341, 144
Krimigis, S. M., Decker, R. B., Roelof, E. C., et al. 2019, NatAs, 3, 997
Lazarian, A., & Yan, H. 2014, ApJ, 784, 38
le Roux, J. A., & Webb, G. M. 2007, ApJ, 667, 930
le Roux, J. A., Zank, G. P., Milano, L. J., & Matthaeus, W. H. 2004, ApJ, 602, 396
Lee, K. H., & Lee, L. C. 2020, ApJ, 904, 66
Lee, K. H., & Lee, L. C. 2019, NatAs, 3, 154
Liu, K., Möbius, E., Gary, S. P., & Winske, D. 2012, JGR, 117, A10102
Luo, X., Potgieter, M. S., Zhang, M., et al. 2016, ApJ, 826, 182
Mace, R. L., Matthaeus, W. H., & Bieber, J. W. 2000, ApJ, 538, 192
Matthaeus, W. H., Bieber, J. W., Ruffolo, D., et al. 2007, ApJ, 667, 956
Minter, A. H., & Spangler, S. R. 1996, ApJ, 458, 194
Opher, M., & Drake, J. F. 2013, ApJL, 778, L26
Pogorelov, N. V., Heerikhuisen, J., Zank, G. P., et al. 2011, ApJ, 742, 104
Qin, G., Matthaeus, W. H., & Bieber, J. W. 2002, GeoRL, 29, 1048
Qin, G., Matthaeus, W. H., & Bieber, J. W. 2006, ApJL, 640, L103
Rankin, J. S., McComas, D. J., & Schwadron, N. A. 2020, ApJ, 895, 103
Rankin, J. S., Stone, E. C., Cummings, A. C., et al. 2019, ApJ, 873, 46
Redfield, S., & Linsky, J. L. 2004, ApJ, 613, 1004
Richardson, J. D., Belcher, J. W., Garcia-Galindo, P., & Burlaga, L. F. 2019, NatAs, 3, 1019
Schlickeiser, R. 1989, ApJ, 336, 243
Schlickeiser, R., & Achatz, U. 1993, JPlPh, 49, 63
Schlickeiser, R., & Miller, J. A. 1998, ApJ, 492, 352
Shalchi, A., Bieber, J. W., Matthaeus, W. H., & Qin, G. 2004, ApJ, 616, 617
Shalchi, A., & Schlickeiser, R. 2004a, ApJ, 604, 861
Shalchi, A., & Schlickeiser, R. 2004b, A&A, 420, 821
Sheng, D., Liu, K., Florinski, V., & Perez, J. D. 2021, ApJ, 922, 271
Stone, E. C., Cummings, A. C., & McDonald, F. B. 2013, Sci, 341, 150
Strauss, R. D., le Roux, J. A., Engelbrecht, N. E., et al. 2016, ApJ, 825, 43
Strauss, R. D., Potgieter, M. S., Ferreira, S. E. S., et al. 2013, ApJL, 765, L18

Tautz, R. C., & Dosch, A. 2013, PhPl, 20, 022302
Usmanov, A. V., Goldstein, M. L., & Matthaeus, W. H. 2016, ApJ, 820, 17
Wallis, M. K., & Dryer, M. 1976, ApJ, 205, 895
Xu, S., & Li, H. 2022, ApJL, 941, L19
Zank, G. P., Du, S., & Hunana, P. 2017, ApJ, 842, 114
Zank, G. P., Nakanotani, M., & Webb, G. M. 2019, ApJ, 887, 116
Zhang, M., & Pogorelov, N. 2020, ApJ, 895, 1
Zirnstein, E. J., Giacalone, J., Kumar, R., et al. 2020, ApJ, 888, 29